Journal of Hazardous Materials Advances 21 (2026) 101064

Contents lists available at ScienceDirect

Journal of Hazardous Materials Advances

journal homepage: www.elsevier.com/locate/hazadv

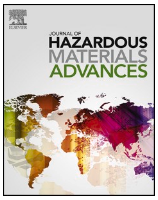

Development of visible-light-active Fe_2O_3-hBN photocatalysts for sustainable degradation of emerging pollutants under simulated sunlight conditions

Mariam Bouziani [a,*], Asmae Bouziani [b,g], Abdelghani Hsini [c], Claudia L. Bianchi [d,e], Ermelinda Falletta [d,e], Giuseppina Cerrato [f], Alessia Giordana [f], Gökhan Çelik [g], Robert Hausler [a]

[a] *STEPPE, École de technologie supérieure, Montreal, Canada*
[b] *Kocaeli University, Department of Chemistry and Chemical Processing Technology, Advance Vocational School of Hereke Asım Kocabıyık, Kocaeli, Turkey*
[c] *Laboratory of Advanced Materials and Process Engineering (LAMPE), Faculty of Science, Ibn Tofail University, BP 133, 14000 Kenitra, Morocco*
[d] *Department of Chemistry, Università degli Studi di Milano, Via C. Golgi 19, 20133 Milan, Italy*
[e] *Consorzio Interuniversitario Nazionale per la Scienza e Tecnologia dei Materiali (INSTM), Via Giusti 9, 50121 Florence, Italy*
[f] *Department of Chemistry, Università degli Studi di Torino, via P. Giunta, 7, 10125 Turin, Italy*
[g] *Middle East Technical University, Chemical Engineering Department, Ankara, Turkey*

ARTICLE INFO

Keywords:
Fe_2O_3-hBN composites
Photocatalysis
Sunlight irradiation
Methylene blue
Ibuprofen
Water treatment
Environmental remediation

ABSTRACT

In this work, Fe_2O_3-hBN composites with different Fe_2O_3 loadings (0.2–2 wt%) were synthesized via a dry impregnation approach and evaluated as sustainable photocatalysts for water purification. The materials were comprehensively characterized using XRD, SEM, TEM, XPS, FTIR, UV–Vis, PL, and N_2 adsorption-desorption analyses to elucidate their structural, optical, and surface properties. Under simulated solar irradiation, the 0.5 wt% Fe_2O_3-hBN composite showed the most efficient photocatalytic activity among the tested materials. Approximately 80% removal of methylene blue and more than 70% degradation of ibuprofen were achieved within 120 min, highlighting the superior performance of this composition. This improvement was attributed to enhanced visible-light absorption and a reduced band gap (2.7 eV). Radical scavenging experiments identified photogenerated holes (h^*) and superoxide radicals (O_3^{*-}) as the main reactive species. The composite exhibited excellent stability and reusability across multiple cycles. These findings highlight Fe_2O_3-hBN as an efficient and eco-friendly photocatalyst for sustainable water remediation applications.

1. Introduction

Environmental pollution by organic contaminants, including synthetic dyes and pharmaceutical compounds, has become a major concern due to their persistence, toxicity, and continuous release into aquatic environments. These pollutants, commonly originating from textile, pharmaceutical, and personal care industries, pose significant ecological and human health risks even at low concentrations (Chakraborty et al., 2023; Khan et al., 2024). Consequently, the development of efficient and sustainable treatment technologies for the removal of such hazardous contaminants from water remains a pressing challenge.

Among advanced water treatment strategies, photocatalytic degradation has emerged as a promising and environmentally friendly approach, as it enables the transformation of organic pollutants into less harmful species by utilizing semiconductor materials and light energy (Mohammed et al., 2023; Navidpour et al., 2024). Solar-driven photocatalysis is particularly attractive because sunlight is abundant, renewable, and cost-free. However, conventional photocatalysts such as TiO_2 and ZnO are limited by their wide band gaps (3.20 and 3.37 eV, respectively), rapid electron-hole recombination, and activation predominantly under ultraviolet irradiation, which accounts for only a small fraction of the solar spectrum. These limitations have motivated extensive research into visible-light-responsive photocatalysts through strategies such as heterojunction construction, surface modification, and composite material design (Ahmadpour et al., 2020).

In this context, two-dimensional (2D) hexagonal boron nitride (hBN) has emerged as a promising support for photocatalytic systems. hBN

---

* Corresponding author.
E-mail address: mariam.bouziani.1@ens.etsmtl.ca (M. Bouziani).

https://doi.org/10.1016/j.hazadv.2026.101064
Received 22 October 2025; Received in revised form 23 December 2025; Accepted 5 February 2026
Available online 6 February 2026

possesses excellent chemical and thermal stability, a layered structure, and a high specific surface area (Cassabois et al., 2016; Sharma et al., 2025). Although its wide band gap (~5.5 eV) prevents intrinsic visible-light photoactivity, hBN can act as an effective support or co-catalyst, facilitating charge migration and suppressing charge recombination when coupled with visible-light-active semiconductors (Gao et al., 2020).

Iron oxide (Fe_2O_3), particularly hematite (α-Fe_2O_3), is a promising visible-light-active photocatalyst owing to its narrow band gap (~2.1 eV), earth abundance, low toxicity, and chemical stability (Kay et al., 2006; Kumar et al., 2022; Arif et al., 2024). Nevertheless, the photocatalytic performance of Fe_2O_3 is often hindered by poor charge carrier separation and particle aggregation, which significantly reduce its efficiency (Sivula et al., 2011). Coupling Fe_2O_3 with a suiTable support material represents an effective strategy to overcome these drawbacks by improving dispersion and interfacial charge transfer (Ren and Innocenzi, 2021).

Combining Fe_2O_3 with hBN to form heterostructured composites offers the potential to integrate the visible-light absorption capability of Fe_2O_3 with the excellent stability and charge-mediation properties of hBN. Despite this promise, Fe_2O_3-hBN systems remain insufficiently explored, particularly at ultra-low Fe_2O_3 loadings where high dispersion and efficient interfacial charge separation are expected to play a critical role. Moreover, systematic investigations addressing the degradation of chemically distinct pollutants using such composites under solar irradiation are still limited.

In our previous work, we demonstrated the potential of 2D hBN as an effective support for visible-light-active photocatalysts, established by Co_3O_4-decorated hBN composites showing enhanced degradation of methylene blue (MB) and ibuprofen (IBP) under visible-light irradiation due to improved interfacial charge separation (Bouziani et al., 2025). Building on these findings, the present study focuses on Fe_2O_3-modified hBN composites as an alternative, iron-based photocatalytic system. MB, a model cationic dye, and IBP, a widely detected pharmaceutical contaminant with different physicochemical properties and degradation pathways, were selected to evaluate the versatility of the photocatalyst.

In this work, Fe_2O_3-hBN composites were synthesized via a facile dry impregnation approach and systematically characterized in terms of structural, optical, and electronic properties. Their photocatalytic performance toward the solar-driven degradation of MB and IBP was investigated, and the effects of Fe_2O_3 loading were analyzed to identify the optimal composition. In addition, radical scavenger experiments were conducted to elucidate the dominant reactive species and gain insight into the photocatalytic mechanism. This study provides a deeper understanding of Fe_2O_3-hBN heterojunctions and highlights their potential for visible-light-driven removal of hazardous organic pollutants from water.

Recent studies have explored hBN-supported metal oxides such as $Co_{3.}O_4$-hBN and Fe_2O_3-hBN, demonstrating that the incorporation of transition-metal oxides onto hBN can enhance visible-light activity through improved charge separation and interfacial electron transport (Bouziani et al., 2025; Sheng et al., 2018). However, most reported systems rely on relatively high oxide loadings, which often lead to nanoparticle agglomeration and reduced photocatalytic efficiency (Ashraf et al., 2024). Moreover, the photocatalytic behavior of Fe_2O_3-hBN composites, particularly at ultra-low Fe_2O_3 contents (<1 wt %), has not been systematically investigated. Compared to these reports, the present work introduces a low-loading Fe_2O_3-hBN composite that achieves efficient degradation of both MB and IBP under simulated sunlight. These gaps and challenges in existing literature highlight the innovation and significance of the Fe_2O_3-hBN system developed here.

2. Materials and methods

Iron(III) nitrate nonahydrate ($Fe(NO_3)_3$ $9H_2O$) and hexagonal boron nitride (hBN, 99.9 % metal basis) were obtained from Aldrich and used as received. Ibuprofen (IBP, ≥98 %) and methylene blue (MB, 97 %) were employed as representative organic contaminants in the photocatalytic experiments and were also sourced from Aldrich.

2.1. Materials synthesis

The Fe_2O_3-hBN composite was prepared using a dry impregnation method adapted from previously reported procedures for metal-oxide deposition on solid supports, with minor modifications to control the Fe_2O_3 loading and dispersion on hBN (Bartholomew and Farrauto, 2010). A series of $Fe(NO_3)_3$ $9H_2O$ precursor solutions was prepared to achieve Fe_2O_3 loadings of 0.2, 0.5, 1.0, and 2.0 wt %. These solutions were gradually added to 1 g hBN in small volumes. After each addition, the partially wet samples were kept in the oven at 100 °C for 15 min. This stepwise impregnation and drying process was repeated until the entire precursor solution had been added. After the final addition, the obtained materials were kept at 100 °C overnight, then calcinated at 500 °C for 3 h to obtain Fe_2O_3-hBN composite. Fe_2O_3 was obtained by dehydrating $Fe(NO_3)_3$ $9H_2O$ at 120 °C for 2 h, followed by calcination at 500 °C for 3 h.

2.2. Characterization

The structural, optical, and textural properties of pristine h-BN and Fe_2O_3-hBN composites were investigated using complementary characterization techniques. Crystalline features were analyzed by powder X-ray diffraction. Phase assignment was performed by matching the experimental diffraction patterns with reference files from the International Centre for Diffraction Data database. The reflections were indexed to hexagonal boron nitride (h-BN; PDF 34–0421) and hematite (α-Fe_2O_3; PDF 33–0664). Fe_2O_3, hBN, and 0.5 % Fe_2O_3-hBN composite (the most performing photocatalyst) crystallite size (d) was determined from the Scherrer formula (Eq.1) (Shiraishi and Inagaki, 2003)

$$d = \frac{K\lambda}{\beta\ cos\theta} \tag{1}$$

where K, λ, β, θ represent shape-related constants, X-ray wavelength (0.15406 nm), full width at half maximum (FWHM), and Bragg angle, respectively.

The optical absorption behavior and charge-carrier recombination characteristics were examined by UV–Vis diffuse reflectance spectroscopy and photoluminescence spectroscopy, respectively. The bandgap energy (E_g) was obtained from the Kubelka-Munk function, as depicted in Eq. (2) (Jaramillo-Páez et al., 2017):

$$A\left(h\nu - E_g\right)^{\frac{n}{2}} = \alpha h\nu \tag{2}$$

Specific surface area and porosity were determined from nitrogen adsorption-desorption measurements following sample outgassing. Morphological features and particle dispersion were evaluated using scanning and transmission electron microscopy. Surface functional groups and bonding environments were identified by Fourier-transform infrared spectroscopy. Additional experimental details, instrumental parameters, and extended characterization data are provided in the Supporting Information.

2.3. Photocatalytic tests

Photocatalytic degradation experiments were conducted using hBN and Fe_2O_3-hBN compounds with varying Fe_2O_3 loadings under simulated solar irradiation. Photocatalytic tests were conducted in a batch reactor employing a 250 mL Pyrex reactor, externally shielded with aluminum foil. For each run, 100 mL of an aqueous solution of MB or IBF at an initial concentration of 10 ppm was used, with a photocatalyst dosage of 1 g/L. Irradiation was provided by an Osram Ultra-Vitalux lamp (300 W), which emits a solar-like spectrum, placed 10 cm above the solution surface. The reactor was equipped with a circulating water jacket to maintain a constant temperature throughout the reaction. Prior to light exposure, the suspension was magnetically stirred in the dark for 20 min to establish adsorption-desorption equilibrium. Photocatalytic reactions were then carried out for 120 min. At predetermined time intervals, 1.5 mL aliquots were withdrawn, filtered through a 0.45 μm regenerated cellulose (RC) membrane, and analyzed. MB concentration was quantified by monitoring the absorbance at $\lambda_{max} = 664$ nm using UV–Vis spectroscopy, whereas IBF concentration was determined by high-performance liquid chromatography (HPLC).

HPLC analyses were performed on a Shimadzu LC-20AD system equipped with dual pumps, an autosampler (SIL-20AC), a column oven (CTO-20A), a photodiode array detector (SPD-M20A), and a refractive index detector (RID-10A). Chromatography analysis was done via a C18 reversed-phase column (4.6 × 150 mm, 5 μm) with a mobile phase consisting of acidified water (pH 2, adjusted with H_3PO_4) and methanol in a 1:4 (v/v) ratio at a flow rate of 1.0 mL/min The column temperature was kept at 50 °C, the injection volume was 20 μL, and IBF detection was carried out at 223 nm using the PDA detector. Data acquisition and processing were carried out with Shimadzu LabSolutions software. To ensure direct comparability of photocatalytic performance between Fe_2O_3 loadings and to focus on the structure-activity relationship, all degradation experiments were carried out under fixed conditions (natural pH, identical catalyst dosage, and identical initial pollutant concentrations). Photolysis experiments under similar irradiation conditions were performed, resulting in negligible degradation of both MB and IBP, confirming the stability of these organic species under simulated solar light illumination.

All photocatalytic degradation experiments were carried out in triplicate under identical conditions, and the results are presented as mean ± standard deviation.

2.4. *Identification of active species*

The dominant reactive species involved in the photocatalytic degradation were examined through scavenger-assisted experiments. Specific quenchers were introduced into the reaction system to selectively suppress individual charge carriers or reactive oxygen species. Potassium iodide (0.3 mM), chloroform (2.4 mM), and isopropyl alcohol (0.5 mM) were employed to inhibit photogenerated holes (h^*), superoxide radicals ($\bullet O_2^-$), and hydroxyl radicals (•OH), respectively. All experiments were conducted under identical photocatalytic conditions using methylene blue as the target pollutant and the 0.5 % Fe_2O_3-hBN composite as the catalyst, with the only modification being the addition of the corresponding scavenger.

3. Results and discussion

3.1. *Characterization*

The crystallinity and phase composition of pure Fe_2O_3, hBN, and the Fe_2O_3-hBN composites were investigated by X-ray diffraction (XRD). XRD patterns are shown in Fig. 1a. The XRD pattern of hBN displays characteristic peaks at approximately 26.6°, 41.5°, 43.6°, 50.2°, and 55.1°, corresponding to the (002), (100), (101), (102), and (004) crystallographic planes of hexagonal boron nitride (hBN), respectively (Zhang et al., 2017). Furthermore, the XRD pattern of Fe_2O_3 reveals peaks at around 24.1°, 33.2°, 35.6°, 40.9°, 49.5°, 54.0°, and 62.5°, which are associated to the (012), (104), (110), (113), (024), (116), and (214) planes of hematite (α- Fe_2O_3) (Liu et al., 2020). These peaks align

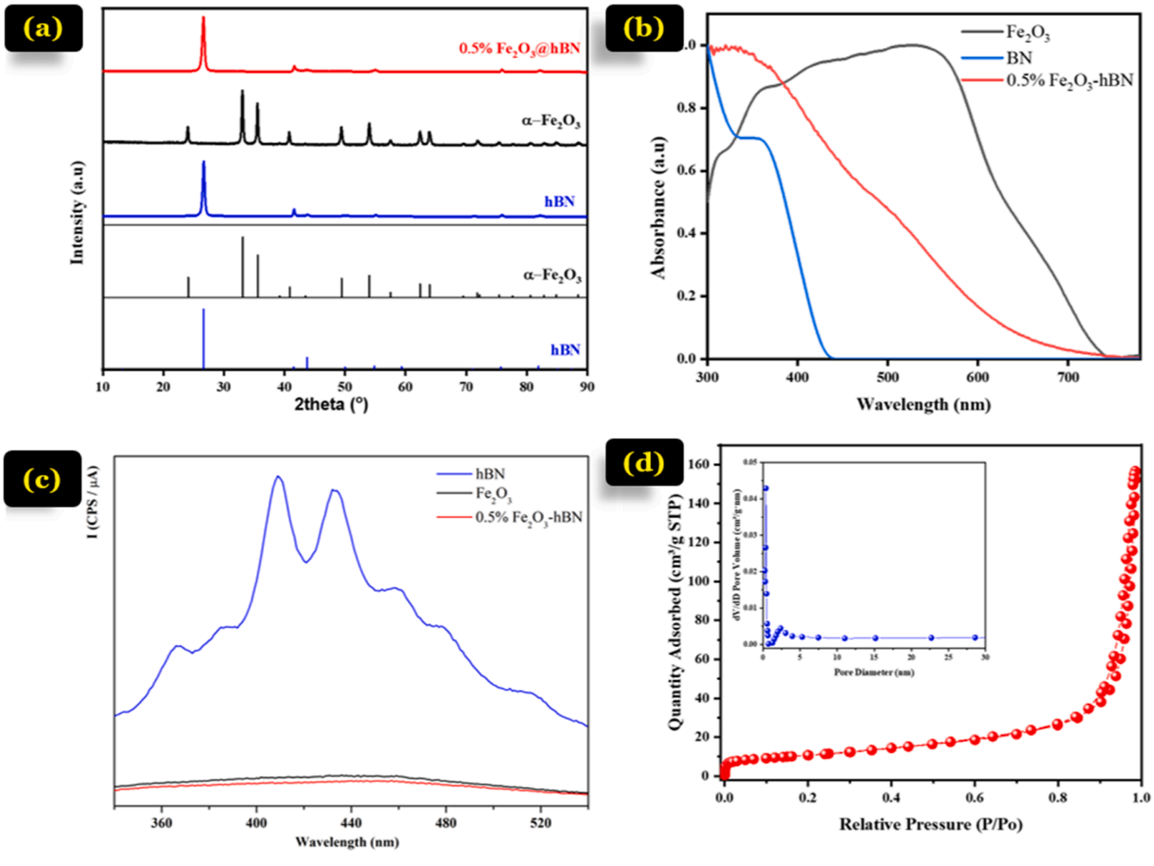

Fig. 1. (a) XRD patterns of α- Fe_2O_3, hBN, and 0.5 % α-Fe_2O_3-hBN. Reference data for h-BN (JCPDS no. 34–0421) and α- Fe_2O_3 (JCPDS no. 33–0664) are included for comparison. (b) UV–vis spectra of α-Fe_2O_3, hBN and 0.5 % Fe_2O_3-hBN. (c) PL spectra of hBN, Fe_2O_3 and 0.5 % Fe_2O_3-hBN. (d) Nitrogen adsorption-desorption isotherm of 0.5 % Fe_2O_3-hBN composite. Inet: pore size of 0.5 % Fe_2O_3-hBN.

with the reference data for α-Fe_2O_3 and confirm that hematite is the dominant phase present. Moreover, the XRD pattern of 0.5 % Fe_2O_3-hBN composite showed only hBN diffraction patterns, because of the low content of Fe_2O_3 (below the typical detection limit of XRD) and high dispersion, as confirmed by the TEM-EDS and FESEM results (Figs. 2 and 3). The average crystallite sizes were calculated using the Scherrer equation, based on the most intense diffraction peaks: the (002) peak for hBN and the (104) peak for Fe_2O_3, and are listed in Table 1. It is noteworthy to mention that the crystallite size remained similar following the addition of Fe_2O_3, indicating effective dispersion of iron oxide on hBN.

The UV–Vis absorbance spectra of Fe_2O_3, hBN, and the 0.5 % Fe_2O_3-hBN composite (Fig. 1b) reveal distinct differences in light absorption properties. Pristine Fe_2O_3 exhibits strong absorption across a wide range, extending into the visible region up to 650 nm, attributed to charge transfer transitions between O 2p orbitals and Fe 3d states, consistent with its relatively small band gap (~2.1 eV) (Boudjemaa et al., 2009). In contrast, hBN shows almost no absorption beyond 400 nm, reflecting its wide band gap and UV-limited activity (Chou et al., 2022). The 0.5 % Fe_2O_3-hBN composite displays an absorption profile similar to Fe_2O_3, with a slight red shift, indicating successful incorporation of Fe_2O_3 onto the hBN matrix. While these results suggest that Fe_2O_3 is the primary contributor to visible light harvesting, the presence of hBN may enhance the separation of photogenerated charges in the composite, potentially improving photocatalytic performance (Shenoy et al., 2021). The bandgap energies of hBN, $Fe_2O_{3,}$ and 0.5 %Fe_2O_3-hBN were estimated from the Kubelka-Munk function, assuming an indirect Eg of hBN is around 5.4 eV (Cassabois et al., 2016; Watanabe et al., 2004; Tarrio and Schnatterly, 1989), while Fe_2O_3 displays an Eg ≈ of 2.1 eV (Young et al., 2013; Ahn et al., 2022). Photoluminescence (PL) spectroscopy was performed to probe the optical properties and defect-related emissions in bare h-BN, Fe_2O_3, and 0.5 %Fe_2O_3-hBN composites. 0.5 %Fe_2O_3-hBN showed a suppression of PL intensity in comparison to hBN and Fe_2O_3, as shown in Fig. 1c. This is consistent with previous reports on PL quenching in metal-oxide/h-BN composites (Zhou et al., 2022). The reduced emission is attributed to charge transfer or non-radiative recombination facilitated by Fe species, which may act as electron traps or introduce surface states that deactivate the emissive centers in hBN (Mani et al., 2020). Although Fe species were not detected in the XPS spectrum or XRD pattern, which is reasonably attributed to the low Fe_2O_3 loading (0.5 wt %), the photoluminescence (PL) spectra of the Fe_2O_3-hBN composite exhibit features consistent with those reported for α-Fe_2O_3-based systems, particularly in terms of absorption-emission behavior. Compared to pristine hBN, the Fe_2O_3-hBN composite shows a noticeable PL quenching effect, indicating a more efficient separation of photogenerated charge carriers.

The suppression of PL intensity suggests a reduction in radiative electron-hole recombination, which can be attributed to the formation of an interfacial charge-transfer pathway between Fe_2O_3 and hBN. In this heterojunction system, photogenerated electrons in Fe_2O_3 are transferred toward the hBN support, while holes remain in the valence band of Fe_2O_3, thereby inhibiting recombination processes. This interpretation is consistent with the enhanced photocatalytic performance observed for the Fe_2O_3-hBN composite under visible-light irradiation. A more detailed discussion of the band alignment and charge-transfer mechanism is provided in the subsequent Mechanism section.

The nitrogen adsorption-desorption isotherms of Fe_2O_3, hBN, and the 0.5 % Fe_2O_3-hBN composite show distinct differences in surface area and porosity. hBN has the highest adsorption capacity and surface area, displaying a Type IV isotherm with an H3 hysteresis loop characteristic of mesoporous structures and mainly micropores (<2 nm) (Fig.S2). Fe_2O_3 exhibits lower adsorption, a broader pore size distribution centered around 20- 40 nm, and a less uniform mesoporous network due to particle agglomeration (Fig.S3). The 0.5 % Fe_2O_3/hBN composite

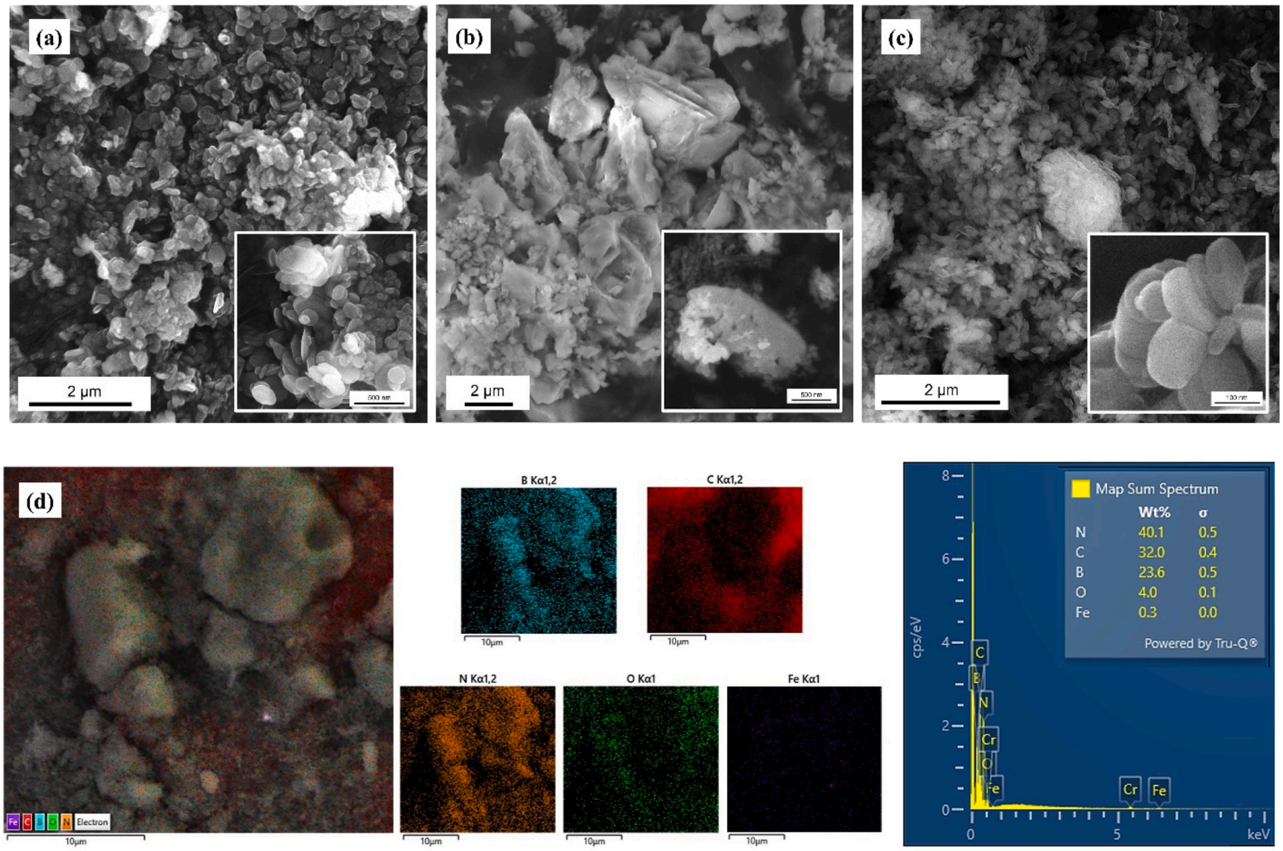

Map Sum Spectrum

	Wt%	σ
N	40.1	0.5
C	32.0	0.4
B	23.6	0.5
O	4.0	0.1
Fe	0.3	0.0

Fig. 2. (a) FESEM images of hBN, (b) Fe_2O_3, (c) 0.5 %Fe_2O_3-BN, (d) elemental mapping and EDS spectrum of 0.5 % Fe_2O_3-hBN.

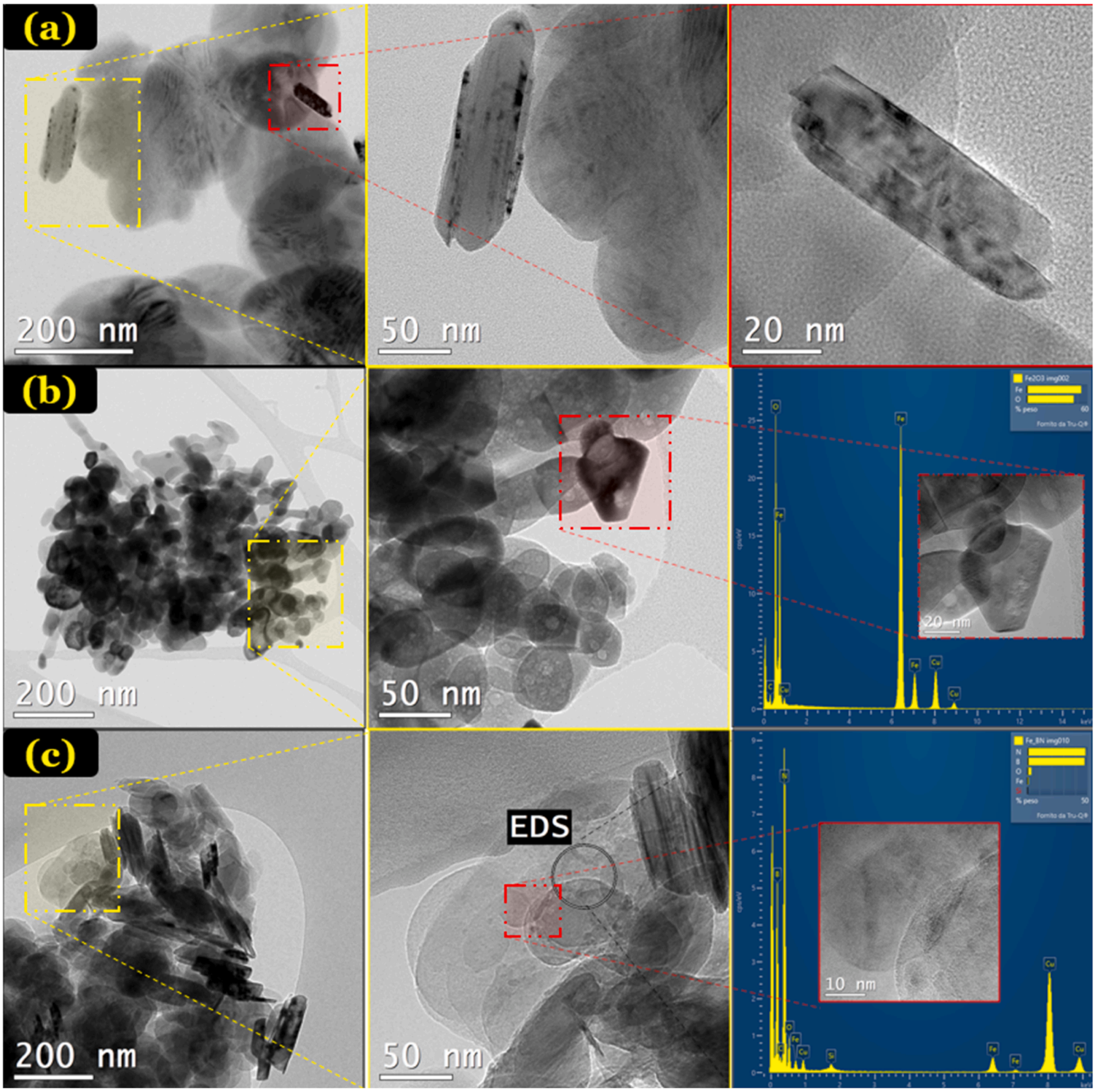

Fig. 3. (a) TEM images of hBN, and TEM images and EDS spectrum of (b) Fe_2O_3, and (c) 0.5 %Fe_2O_3-hBN.

Table 1
Physico-chemical properties of hBN, Fe_2O_3, and 0.5 %Fe_2O_3-hBN.

Samples	Crystallite size D (nm)	S_{BET} (m^2/g)	Pore volume (cm^3/g)	Pore size (nm)	Eg (eV)
hBN	28.0	32.0	0.21	25.0	5.3
Fe_2O_3	39.3	15.2	0.10	22.1	2.1
0.5 % Fe_2O_3-hBN	30.0	38.0	0.24	22.0	2.7

maintains the mesoporous nature of hBN but with slightly reduced surface area (38.0 m^2/g) and increased pore volume (0.24 cm^3/g), indicating well-dispersed Fe_2O_3 that introduces additional meso-porosity without blocking pores (Fig.1d). Pure Fe_2O_3 has a BET surface area of 15.2 m^2/g, pore volume 0.10 cm^3/g, and larger pores (~22.1 nm), while pure hBN shows 32.0 m^2/g surface area, 0.21 cm^3/g pore volume, and pores (~25 nm). Overall, Fe_2O_3 addition increases surface area but enhances pore volume and retains the mesoporous structure, expectedly beneficial for catalytic applications.

The FTIR spectra of α-Fe_2O_3, hBN, and the 0.5 % Fe_2O_3-hBN composite are given in Fig.S4. The bare hBN spectrum shows two prominent peaks in the range of 1300 - 800 cm^{-1}, corresponding to the B-N stretching and B-N-B bonding modes, typical of hBN (Zhang et al., 2020). In the case of α-Fe_2O_3, characteristic peaks at around 550 cm^{-1} are observed, which are attributed to the Fe-O stretching vibrations in the hematite structure (Battisha et al., 2006). For the 0.5 % Fe_2O_3-hBN composite, the infrared spectrum was dominated by the characteristic vibrational modes of h-BN, with bands observed at approximately 1400 cm^{-1} corresponding to B-N stretching and near 800 cm^{-1} assigned to B-N bending vibrations. No distinct absorption features attribuTable to Fe_2O_3 were detected. This observation is reasonably attributed to the extremely low iron oxide loading, which likely falls below the sensitivity limit of FTIR spectroscopy, resulting in signals too weak to be resolved against the intense h-BN framework bands (Nakamoto, 2008).

The general morphology of pristine hBN and Fe_2O_3 materials, as well as that of the 0.5 % Fe_2O_3-hBN composite, was investigated by field emission SEM (FESEM). hBN (Fig.2a) exhibits a layered structure, typical of the hexagonal boron nitride material (Kar et al., 2021), whereas Fe_2O_3 (Fig.2b) appears as made up of aggregated (nano)particles, with a lot of irregularity in both shape and size for the aggregates. In the 0.5 % Fe_2O_3-hBN composite (Fig.2c), Fe_2O_3 nanoparticles are expected to be well-dispersed across the BN matrix, but this morphological feature is hardly visible in the FESEM images, even at high magnification (see the inset to Fig. 2c). This might, in any case, suggest that the composite synthesis successfully prevented Fe_2O_3 agglomeration and will be further confirmed by TEM (Fig. 3). The elemental mapping and the EDS spectrum (Fig. 2d) indicate the targeted loading is achieved and the presence of all the expected elements (Fe, B, N, O, and C) in the composite, confirming the successful addition of Fe_2O_3 into the hBN matrix.

Electron microscopy imaging studies at the nanoscale through TEM (and EDS analyses thereof) reveal the successful incorporation of Fe_2O_3 nanoparticles into the BN matrix. TEM images of BN (Fig.3a) show well-organized, layered sheets with a general hexagonal shape, whereas the Fe_2O_3 sample (Fig. 3b) exhibits typical nanoparticle aggregation, with particle sizes ranging in the nanoscale, from 10 to 50 nm. The EDS spectrum confirms its elemental composition made of Fe and O, as expected. In the 0.5 % Fe_2O_3-hBN composite (Fig. 3c), Fe_2O_3 nanoparticles are well dispersed across and on top of the BN sheets, indicating the successful synthesis that prevented aggregation among the Fe_2O_3 nanoparticles themselves. Moreover, the EDS spectrum supports the presence of the expected elements (B, N, Fe, and O) at the nanoscale, indicating the highly uniform nature of the material.

XPS was used to investigate the surface chemical composition of the hBN and 0.5 % Fe_2O_3-hBN composite. In both samples (Fig. 4a and Fig. S5), the deconvolution of B 1 s exhibited a primary peak at ∼190.5 eV corresponding to B-N bonding, confirming the presence of hBN. A secondary peak at ∼192.0 eV was observed in both samples and is attributed to oxidized boron (B-O), with slightly higher intensity in the Fe_2O_3-hBN, suggesting enhanced surface oxidation or possible interaction with Fe species (Tay et al., 2014; Liu et al., 2022). Similarly, the deconvolution of the N 1 s spectrum displayed a peak at ∼398.5–399.5 eV in both samples, attributed to sp^2-hybridized nitrogen in the BN lattice, while a minor shoulder at ∼401 eV was more pronounced in the composite may result from Fe-induced surface states or N—O bonding (Tay et al., 2014). The C 1 s spectrum of bare h-BN revealed a single peak at ∼284.5 eV due to adventitious carbon (Barr and Seal, 1995; Han et al., 2019), whereas the composite displayed additional features at ∼286.0 and ∼288.5 eV, associated with C—O and CO_3^{2-} species, likely originating from surface hydroxylation or interaction with Fe_2O_3 (Sheng et al., 2018; Han et al., 2019). Deconvolution of the O 1 s spectrum in Fe_2O_3-hBN (Fig. 4d) revealed a broad peak centered at ∼530.1 eV with a shoulder at ∼531.8 eV, attributed to lattice oxygen and surface hydroxyls, respectively (Ashraf et al., 2024). Despite the absence of a detecTable Fe 2p signal consistent with low Fe_2O_3 loading (0.5 wt. %) and surface sensitivity limitations, the methodologies described in Biesinger et al. provide clear evidence that Fe signals often become attenuated or overlapped when Fe is encapsulated or present at low concentrations (Biesinger et al., 2011). The deconvolved spectra of B, N, and O core-levels still capture subtle chemical interactions, supporting the idea that Fe_2O_3 incorporation modifies surface chemistry via mild oxidation and potential Fe-O-B or Fe-N interfacial interactions.

3.2. Photocatalytic experiments

3.2.1. MB and Ibuprofen degradation

The photocatalytic degradation of methylene blue (MB) was evaluated using pristine Fe_2O_3 and Fe_2O_3-hBN composites with different Fe_2O_3 loadings (0, 0.2, 0.5, 1, and 2 wt %) under simulated solar light irradiation. A preliminary screening of all Fe_2O_3 loadings (0.2–2 wt %)

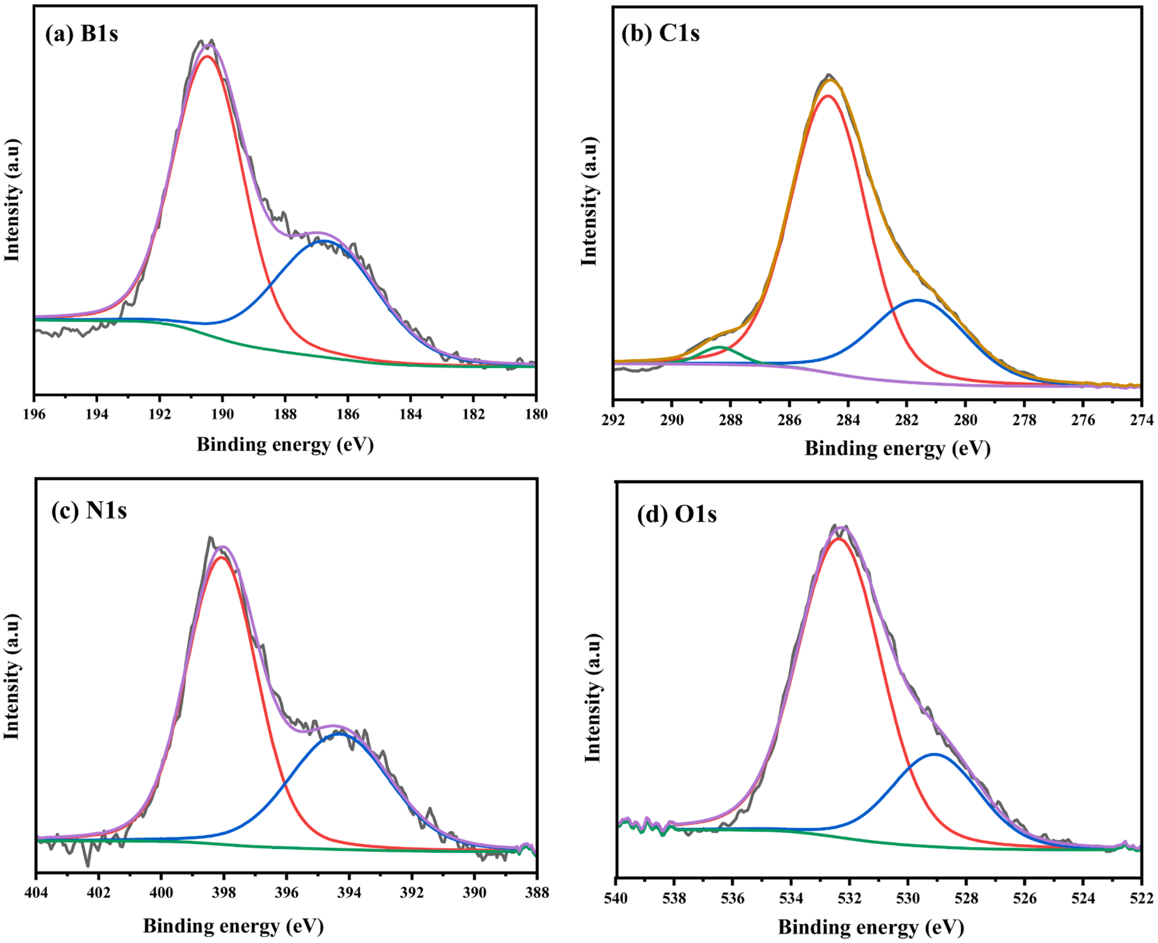

Fig. 4. High-resolution spectra of (a) B 1 s, (b), C 1 s, (c) N 1 s, and (d) O 1 s for 0.5 % Fe_2O_3-hBN composite.

revealed a clear performance trend. The composite containing 0.2 wt % Fe_2O_3 exhibited insufficient surface coverage and weak photocatalytic activity, whereas the 0.5 wt % Fe_2O_3-hBN sample achieved optimal dispersion and the highest degradation efficiency. In contrast, higher Fe_2O_3 loadings (1–2 wt %) resulted in reduced photocatalytic performance, which can be attributed to partial nanoparticle agglomeration and light-shielding effects. Based on these results, detailed structural, optical, and mechanistic characterizations in this work were focused on the optimal 0.5 wt % Fe_2O_3-hBN composite.

As shown in Fig. 5, all Fe_2O_3-loaded hBN composites exhibited enhanced photocatalytic activity compared to pristine Fe_2O_3 and bare hBN, indicating a clear synergistic interaction between Fe_2O_3 and the hBN support. Among the tested samples, the 0.5 wt % Fe_2O_3-hBN demonstrated the highest photocatalytic efficiency, reaching approximately 80 % MB degradation within 120 min of simulated solar light irradiation.

The pseudo-first-order kinetic analysis (Fig. 5b) further supports these results, with the 0.5 % Fe_2O_3-hBN sample exhibiting the highest apparent rate constant, confirming the fastest degradation kinetics. This higher performance can be attributed to an optimum steadiness among number of active Fe_2O_3 sites and high surface area of hBN, which maximizes interfacial contact and promotes efficient charge separation while suppressing electron-hole recombination.

When the Fe_2O_3 loading was increased beyond this optimal value, a gradual decrease in photocatalytic efficiency was observed. This decline is attributed to two main factors: (i) increased particle-particle contact and local aggregation at higher Fe_2O_3 contents, which reduces the effective Fe_2O_3-hBN interfacial area and enhances charge recombination, and (ii) partial surface coverage and light-shielding effects, which limit light penetration and reduce the accessibility of active sites. Conversely, at very low Fe_2O_3 loading (0.2 %), the number of available active sites is insufficient to fully exploit the synergistic interaction, resulting in lower degradation efficiency.

A similar trend was observed for IBP photodegradation under simulated solar light irradiation. As demonstrated in Fig. 5c and Fig. 5d, the 0.5 % Fe_2O_3-hBN composite exhibited the highest performance, completing more than 70 % IBP removal, whereas pristine Fe_2O_3 and hBN showed significantly lower efficiencies. These results further confirm the synergistic interaction between Fe_2O_3 and hBN across pollutants with different chemical structures.

Control experiments performed under identical irradiation conditions in the absence of a catalyst resulted in only negligible photolysis for both MB and IBP, confirming that direct sunlight-driven degradation is minimal and that the observed removal originates predominantly from the photocatalytic activity of the Fe_2O_3-hBN composites.

To contextualize the photocatalytic activity of the optimized 0.5 wt

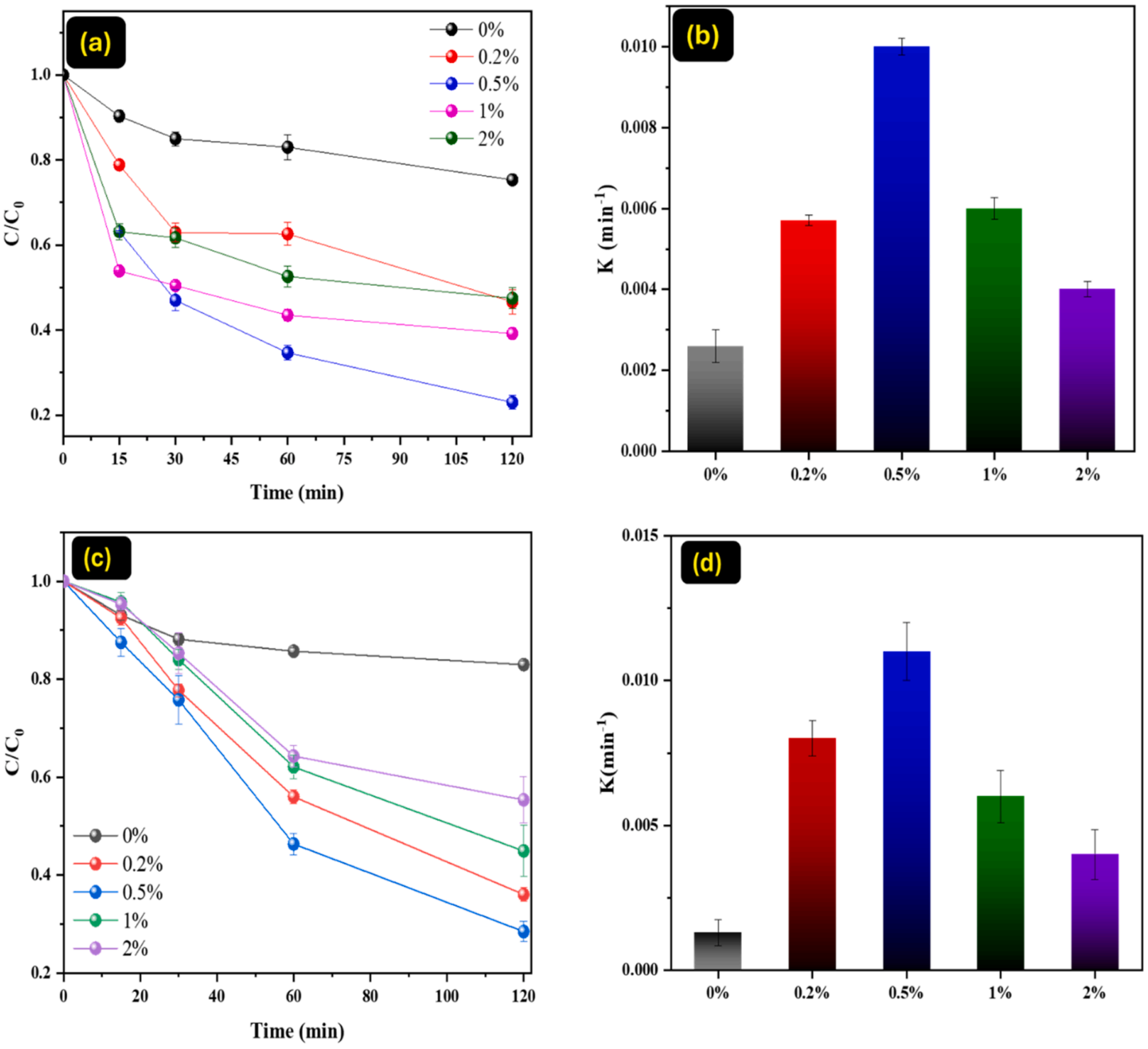

Fig. 5. Photocatalytic performance of the synthesized materials under simulated solar irradiation: (a) methylene blue degradation profiles for h-BN and Fe_2O_3-hBN composites; (b) corresponding apparent rate constants (k, min^{-1}); (c) ibuprofen degradation profiles in the presence of h-BN and Fe_2O_3-hBN composites; and (d) corresponding apparent rate constants (k, min^{-1}).

% Fe_2O_3-hBN composite, a comparison with representative Fe_2O_3 and hBN-based photocatalysts reported in the literature is provided in Table 2. The Table shows that the Fe_2O_3-hBN composite exhibits competitive degradation performance under simulated solar-light irradiation compared to many reported Fe_2O_3-based heterojunctions, confirming its potential as an efficient photocatalyst for environmental purification.

3.2.2. *Photocatalyst stability*

To effectively exhibit the structural stability of the 0.5 % Fe_2O_3-hBN photocatalyst, the structural characteristics of the spent photocatalyst, after one photocatalytic cycle, were examined using XRD, with the results illustrated in Fig. 6a. The diffraction profile of the spent sample shows no obvious changes relative to that of the pristine composite, indicating that the crystalline framework remains intact during the photocatalytic process.

3.3. *Role of reactive species in the degradation process*

The role of reactive oxygen species in the MB photocatalytic degradation using the most promising photocatalyst (0.5 % Fe_2O_3-hBN) was investigated through scavenger experiments. Fig. 6b illustrates the effect of introducing selective radical scavengers on the photocatalytic degradation of methylene blue. For comparison, a reference experiment conducted in the absence of any scavenger was also included and showed an 80 % MB removal. The significant decrease in degradation efficiency upon the addition of $CHCl_3$, a superoxide radical (O_2^{*-}) scavenger, indicates that O_2^{*-} plays a pivotal role in the photodegradation process. A similar trend was observed by the addition of IPA as a hydroxyl radical (OH) scavenger, though to a lesser extent, suggesting that $^{\bullet}OH$ radicals contribute to the degradation mechanism as well. Moreover, the addition of KI, a hole (h*) scavenger, resulted in a marked decline in photocatalytic performance, underscoring the importance of photogenerated holes in the reaction. These findings suggest that the MB degradation in the presence of Fe_2O_3-hBN involves a synergistic effect of O_2^{*-}, $^{\bullet}OH$ radicals, and h*, with superoxide radicals and photogenerated holes being the dominant active species.

3.4. *Photocatalytic reaction pathway using 0.5 % Fe_2O_3-hBN*

Based on the scavenger-assisted tests, the photocatalytic behavior of the 0.5 wt % Fe_2O_3-hBN composite is mainly ruled by superoxide radicals (O_2^{*-}) and photogenerated holes (h*), which play the dominant roles in the degradation process. The moderate decrease in photodegradation efficiency observed in the presence of isopropanol (IPA) indicates that hydroxyl radicals (•OH) also participate in the reaction, although to a lesser extent.

The relatively moderate photoluminescence (PL) quenching observed for the 0.5 wt % Fe_2O_3-hBN composite is consistent with previous reports on low-loading metal oxide/2D-material heterojunctions, where enhanced photocatalytic activity arises mainly from interfacial charge transfer rather than pronounced changes in PL intensity (Sheng et al., 2018; Ashraf et al., 2024; Han et al., 2019). In such systems, the limited semiconductor content often results in modest PL sensitivity, while efficient charge migration across the heterointerface still effectively suppresses charge recombination and enhances photocatalytic performance.

Based on these results, a plausible photocatalytic degradation mechanism for MB is proposed in Fig. 7. To correlate the observed photocatalytic behavior with the electronic structure of the Fe_2O_3-hBN composite, the conduction band (CB) and valence band (VB) positions were estimated using the electronegativity method (Butler, 1977; Yang et al., 2016). Using the experimentally determined band gap of the composite (Eg = 2.7 eV) and the absolute electronegativity of Fe_2O_3 ($X = 5.88$ eV) (Yang et al., 2016), the CB and VB positions were calculated to be +0.03 eV and +2.73 eV versus the normal hydrogen electrode (NHE), respectively. These values are in good agreement with reported band-edge positions of α-Fe_2O_3 (CB ≈ +0.3 eV, VB ≈ +2.4 eV).

In contrast, hBN exhibits a wide band gap of approximately 5.3 eV, with a much more negative conduction band (≈ −1.30 eV) and a deep valence band (≈ +4.00 to +4.20 eV) (Harikrishnan et al., 2024; Pakdel et al., 2014) . This staggered band alignment facilitates efficient interfacial charge separation, whereby photogenerated electrons in Fe_2O_3 are transferred to the more negative CB of hBN, enabling the reduction of dissolved oxygen to superoxide radicals (O_2^{*-}), while the photogenerated holes remaining in the VB of Fe_2O_3 participate in oxidation reactions leading to MB and IBP degradation. This charge-transfer pathway is fully consistent with the scavenger experiment results and explains the enhanced photocatalytic activity of the Fe_2O_3-hBN composite under visible-light irradiation (Fig. 7b).

Specifically, upon light irradiation, Fe_2O_3 absorbs photons and generates electron-hole pairs via excitation of electrons from the VB to the CB (Eq. (3)). The photogenerated electrons are subsequently transferred to hBN and react with dissolved oxygen to form O_2^{*-} radicals (Eq. (4)). Simultaneously, the photogenerated holes can oxidize water molecules to produce •OH radicals (Eq. (5)) or react with hydroxide ions (OH^-) to generate additional •OH species (Eq. (6)). These reactive oxygen species (O_2^{*-} and •OH), together with the direct oxidative action of h^+, synergistically attack and degrade MB molecules into smaller intermediate products and ultimately mineralized species (Eq. (7)).

In summary, the photocatalytic activity of 0.5 % Fe_2O_3-hBN is principally governed by the generation of O_2^{*-}, with photogenerated h^+ and ·OH acting as secondary contributors to the MB degradation.

$$Fe_2O_3 + h\nu \rightarrow e^-_{CB} + \ h^+_{VB} \tag{3}$$

Table 2
Photocatalytic performances of the best material fabricated in the present manuscript and other data reported in the scientific literature.

Photocatalyst	Target pollutant	Light source	Key conditions	Photocatalytic performance	Reference
Fe_2O_3-hBN (0.5 wt %)	MB (10 mg L^{-1}), IBP (10 mg L^{-1})	Simulated sunlight (300 W)	100 mg catalyst, 120 min	MB ≈ 80 %; IBP ≈ 70 %	This work
α-Fe_2O_3 nanoparticles	MB (10 mg L^{-1})	Visible light	50 mg, 120 min	~63 % MB degradation	(Sheng et al., 2018)
Fe_2O_3/hBN nanocomposite	RhB (10 mg L^{-1})	Visible light	30 mg, 120 min	~72 % RhB degradation	(Sheng et al., 2018)
Fe_2O_3/graphene oxide	MB (20 mg L^{-1})	Visible light	20 mg, 90 min	~80 % MB degradation	(Ashraf et al., 2024)
α-Fe_2O_3/g-C_3N_4 heterostructure	Methyl orange (MO)	Visible light	Varied (see ref.)	Enhanced degradation vs. pristine components	(Khurram et al., 2022)
Z-scheme Fe_2O_3/g-C_3N_4 composite	Organic dyes	Visible light	Varied (see ref.)	Improved photocatalytic activity via Z-scheme charge transfer	(Zhang et al., 2026)
α-Fe_2O_3/TiO_2	MB (10 mg L^{-1})	Visible light	30 mg, 120 min	~85 % MB degradation	(Cao et al., 2020)
Fe_2O_3/CQDs	IBP (15 mg L^{-1})	Visible light	30 mg, 120 min	~76 % IBP degradation	(Zhang et al., 2020)
Pani-FeCuCeO_2	MB (20 mg L^{-1})	Visible light	25 mg, 120 min	~79.2 % MB degradation	(Madi et al., 2025)
Fe_2O_3/MoS_2	AB113 (20 mg L^{-1})	Visible light	30 mg, 45 min	~20 % AB113 degradation	(Bagheri and Chaibakhsh, 2021)
Fe_2TiO_5/rGO(10 %)	MB (10 mg L^{-1})	Visible light	50 mg 150 min	~55 % MB degradation	(Guediri et al., 2020)

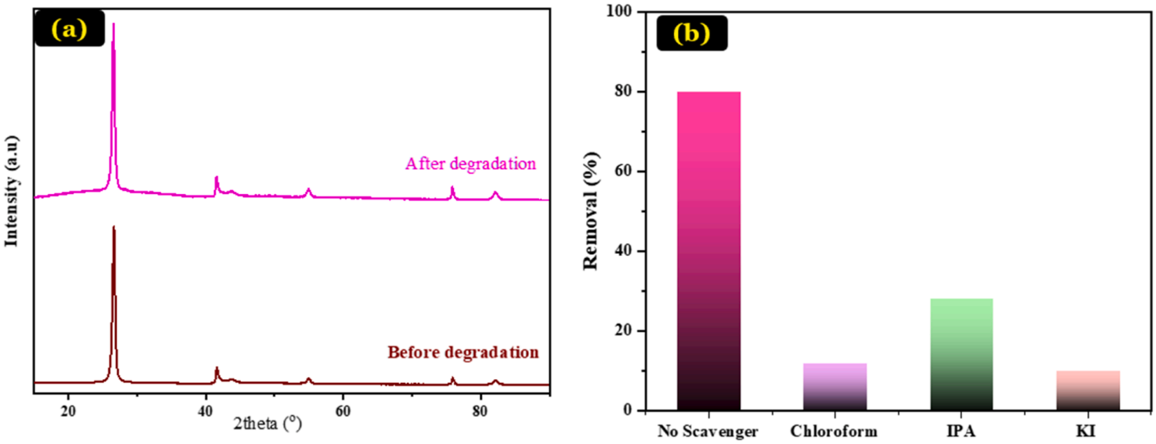

Fig. 6. a) XRD patterns of 0.5 % Fe_2O_3-hBN photocatalyst before and after photocatalytic reaction. b). Photocatalytic degradation of MB using a 0.5 % Fe_2O_3-hBN composite under simulated sunlight in the presence of scavengers: KI (0.3 mM), IPA (0.5 mM), and $CHCl_3$ (2.4 mM).

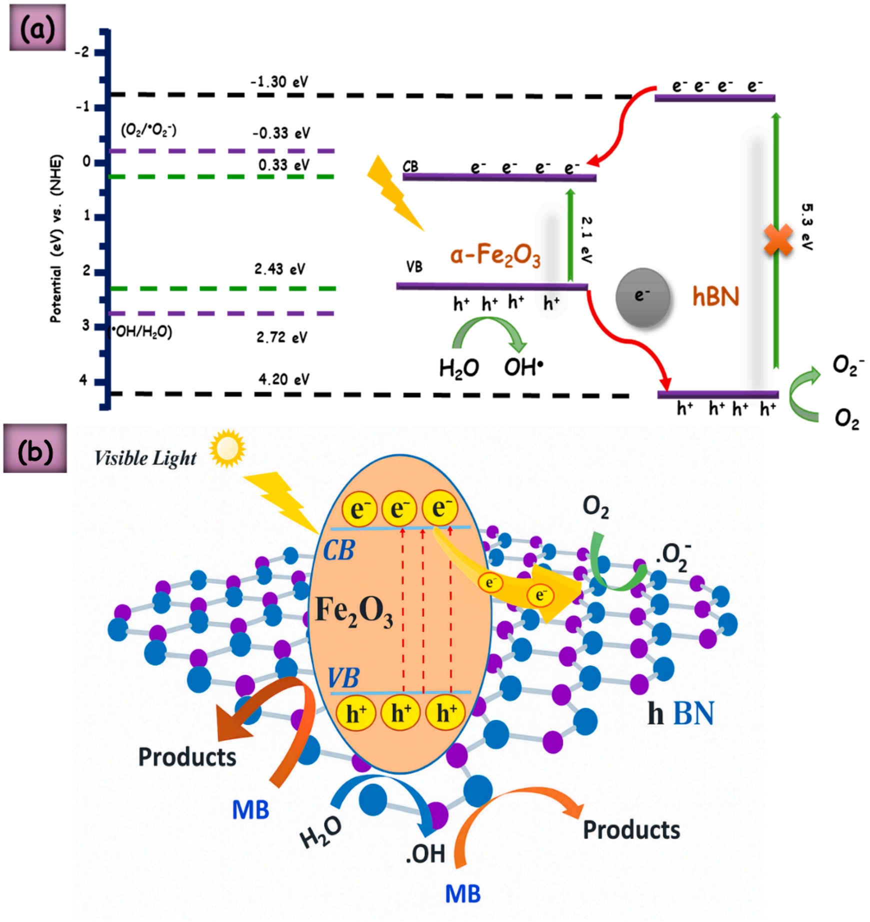

Fig. 7. (a) Schematic illustration of the band structure alignment of the Fe_2O_3-hBN composite; (b) proposed photocatalytic reaction pathway for methylene blue degradation over the 0.5 % Fe_2O_3-hBN photocatalyst.

$$e^- + O_2 \rightarrow O_2^{\cdot -} \quad (4)$$

$$h^+ + H_2O \rightarrow OH^{\cdot} + H^+ \quad (5)$$

$$h^+ + OH^- \rightarrow OH^{\cdot} \quad (6)$$

$$O_2^{\cdot -}/OH^{\cdot}/h^+ + MB \rightarrow Intermediates \rightarrow CO_2 + H_2O \quad (7)$$

4. Conclusion

In this work, Fe_2O_3-hBN composites with varying Fe_2O_3 loadings were successfully synthesized via a dry impregnation method. Comprehensive characterization confirmed the effective incorporation and well dispersion of Fe_2O_3 nanoparticles on the hBN matrix, resulting in modified surface chemistry and enhanced optical properties. Photocatalytic tests demonstrated that the 0.5 % Fe_2O_3-hBN composite exhibited the highest efficiency for degrading both MB and IBP under simulated sunlight irradiation, attributed to an optimal balance between active site availability and the surface area of the support (hBN). Scavenger-assisted experiments indicate that superoxide radicals and photogenerated holes make the primary contributions to the degradation pathway, whereas hydroxyl radicals participate to a lesser extent. Overall, the Fe_2O_3-hBN composite represents a promising photocatalyst for simulated sunlight-driven environmental remediation, combining the advantageous properties of both Fe_2O_3 and hBN to overcome their limitations. Despite the promising photocatalytic performance demonstrated under controlled laboratory conditions, several challenges must be addressed for practical application. The presence of competing ions, natural organic matter, and complex matrices in real wastewater may influence degradation efficiency and requires further investigation. In addition, efficient catalyst separation and recovery strategies, as well as extended multi-cycle reusability studies, are essential to evaluate long-term stability and economic feasibility. Future work will therefore focus on testing the Fe_2O_3-hBN composite in real wastewater systems and developing practical recovery approaches to facilitate its potential application in environmental remediation.

Funding statement

The authors declare that no funds, grants, or other support were received during the preparation of this manuscript.

CRediT authorship contribution statement

Mariam Bouziani: Writing – original draft, Methodology, Investigation, Conceptualization. **Asmae Bouziani:** Writing – original draft, Investigation, Conceptualization. **Abdelghani Hsini:** Writing – review & editing, Investigation. **Claudia L. Bianchi:** Writing – review & editing, Resources. **Ermelinda Falletta:** Writing – review & editing, Resources, Investigation. **Giuseppina Cerrato:** Writing – review & editing, Resources, Investigation. **Alessia Giordana:** Writing – review & editing, Resources, Investigation. **Gökhan Çelik:** Writing – review & editing, Resources, Conceptualization. **Robert Hausler:** Supervision, Methodology.

Declaration of competing interest

The authors declare that they have no known competing financial interests or personal relationships that could have appeared to influence the work reported in this paper.

Acknowledgment

The authors acknowledge the Unitech COSPECT Transmission Electron Microscopy facility of the University of Milan (Italy) for the TEM analyses.

Supplementary materials

Supplementary material associated with this article can be found, in the online version, at doi:10.1016/j.hazadv.2026.101064.

Data availability

Data will be made available on request.

References

Ahmadpour, N., Sayadi, M.H., Sobhani, S., Hajiani, M., 2020. A potential natural solar light active photocatalyst using magnetic ZnFe2O4 @ TiO2/Cu nanocomposite as a high performance and recyclable platform for degradation of naproxen from aqueous solution. J. Clean. Prod. 268, 122023. https://doi.org/10.1016/J.JCLEPRO.2020.122023.

Ahn, H.J., Kment, S., Naldoni, A., Zbořil, R., Schmuki, P., 2022. Band gap and morphology engineering of hematite nanoflakes from an ex situ sn doping for enhanced photoelectrochemical water splitting. ACS Omega 7, 35109–35117. https://doi.org/10.1021/ACSOMEGA.2C04028/SUPPL_FILE/AO2C04028_SI_001.PDF.

Arif, N., Zafar, M.N., Batool, M., Humayun, M., Iqbal, M.A., Younis, M., Li, L., Li, K., Zeng, Y.J., 2024. Recent advances and perspectives on iron-based photocatalysts. J. Mater. Chem. C. Mater. 12, 12653–12691. https://doi.org/10.1039/D4TC01062K.

Ashraf, A., Wahab, R., Al-Khedhairy, A.A., Khan, A., Rahman, F., 2024. Magnetically separable and visible light-driven photocatalytic activity of graphene oxide based α-Fe2O3 nanocomposite. Mater. Chem. Phys. 316, 129111. https://doi.org/10.1016/J.MATCHEMPHYS.2024.129111.

Bagheri, F., Chaibakhsh, N., 2021. Efficient visible-light photocatalytic ozonation for dye degradation using Fe2O3/MoS2 nanocomposite. Sep. Sci. Tech. (Philadelphia) 56, 3022–3032. https://doi.org/10.1080/01496395.2020.1861018;PAGE:STRING:ARTICLE/CHAPTER.

Barr, T.L., Seal, S., 1995. Nature of the use of adventitious carbon as a binding energy standard. J. Vac. Sci. Tech. A 13, 1239–1246. https://doi.org/10.1116/1.579868.

Bartholomew, C.H., Farrauto, R.J., 2010. Fundamentals of industrial catalytic processes: second edition. Fundament. Indust. Catal. Process. Sec. Edn. 1–966. https://doi.org/10.1002/9780471730071;JOURNAL:JOURNAL:BOOKS;WGROUP:STRING:PUBLICATION.

Battisha, I.K., Afify, H.H., Ibrahim, M., 2006. Synthesis of Fe2O3 concentrations and sintering temperature on FTIR and magnetic susceptibility measured from 4 to 300 K of monolith silica gel prepared by sol-gel technique. J. Magn. Magn. Mater. 306, 211–217. https://doi.org/10.1016/J.JMMM.2006.01.251.

Biesinger, M.C., Payne, B.P., Grosvenor, A.P., Lau, L.W.M., Gerson, A.R., Smart, R.S.C., 2011. Resolving surface chemical states in XPS analysis of first row transition metals, oxides and hydroxides: cr, Mn, Fe, Co and Ni. Appl. Surf. Sci. 257, 2717–2730. https://doi.org/10.1016/J.APSUSC.2010.10.051.

Boudjemaa, A., Boumaza, S., Trari, M., Bouarab, R., Bouguelia, A., 2009. Physical and photo-electrochemical characterizations of α-Fe2O3. Application for hydrogen production. Int. J. Hydro. Energy 34, 4268–4274. https://doi.org/10.1016/J.IJHYDENE.2009.03.044.

Bouziani, M., Bouziani, A., Hsini, A., Bianchi, C.L., Falletta, E., Di Michele, A., Çelik, G., Hausler, R., 2025. Synergistic photocatalytic degradation of methylene blue and ibuprofen using Co_2O_4-Decorated hexagonal boron nitride (hBN) composites under Sun-like irradiation. Chemosphere 371, 144061. https://doi.org/10.1016/J.CHEMOSPHERE.2025.144061.

Butler, M.A., 1977. Photoelectrolysis and physical properties of the semiconducting electrode WO2. J. Appl. Phys. 48, 1914–1920. https://doi.org/10.1063/1.323948.

Cao, Y.Q., Zi, T.Q., Zhao, X.R., Liu, C., Ren, Q., Bin Fang, J., Li, W.M., Li, A.D., 2020. Enhanced visible light photocatalytic activity of Fe2O3 modified TiO2 prepared by atomic layer deposition. Sci. Rep. 2020 10:1 10, 13437. https://doi.org/10.1038/s41598-020-70352-z. -.

Cassabois, G., Valvin, P., Gil, B., 2016. Hexagonal boron nitride is an indirect bandgap semiconductor. Nat. Photon. 10, 262–266. https://doi.org/10.1038/NPHOTON.2015.277;TECHMETA=125,140;SUBJMETA=119,301,399,624,639;KWRD=CONDENSED-MATTER+PHYSICS,OPTICAL+MATERIALS+AND+STRUCTURES.

A. Chakraborty, S. Adhikary, S. Bhattacharya, S. Dutta, S. Chatterjee, D. Banerjee, A. Ganguly, P. Rajak, Pharmaceuticals and personal care products as emerging environmental contaminants: prevalence, toxicity, and remedial approaches, ACS Chemical Health and Safety 30 (2023) 362–388. https://doi.org/10.1021/ACS.CHAS.3C00071/ASSET/IMAGES/MEDIUM/HS3C00071_0010.GIF.

Chou, S.L., Lin, M.Y., Huang, T.P., Lin, S.Y., Yang, M.Z., Lee, Y.Y., Wu, Y.J., 2022. Far-UV spectroscopy of mono- and multilayer hexagonal boron nitrides. Spectrochim. Acta A Mol. Biomol. Spectrosc. 270, 120849. https://doi.org/10.1016/J.SAA.2021.120849.

Gao, X., Yao, Y., Meng, X., 2020. Recent development on BN-based photocatalysis: a review. Mater. Sci. Semicond. Process. 120, 105256. https://doi.org/10.1016/J.MSSP.2020.105256.

Guediri, M.K., Chebli, D., Bouguettoucha, A., Bourzami, R., Amrane, A., 2020. Novel Fe2TiO5/reduced graphene oxide heterojunction photocatalyst with improved adsorption capacity and visible light photoactivity: experimental and DFT approach. Environ. Sci. Poll. Res. 2020 28:7 28, 8507–8519. https://doi.org/10.1007/S11356-020-11221-0.

Han, T., Wei, Y., Jin, X., Jiu, H., Zhang, L., Sun, Y., Tian, J., Shang, R., Hang, D., Zhao, R., 2019. Hydrothermal self-assembly of α-Fe 2 O 3 nanorings@graphene aerogel composites for enhanced Li storage performance. J. Mater. Sci. 54, 7119–7130. https://doi.org/10.1007/S10853-019-03371-5/METRICS.

Harikrishnan, K., Hoque, A., Patel, R., Singh, V.P., Gaur, U.K., Sharma, M., 2024. Electronic, electrical, and optical properties of hexagonal boron nitride. Hexag. Boron Nitr. Synt. Prop. Appl. 89–123. https://doi.org/10.1016/B978-0-443-18843-5.00019-7.

Jaramillo-Páez, C., Navío, J.A., Hidalgo, M.C., Bouziani, A., El Azzouzi, M., 2017. Mixed α-Fe2O3/Bi2WO6 oxides for photoassisted hetero-Fenton degradation of Methyl Orange and Phenol. J. Photochem. Photobiol. A Chem. 332, 521–533. https://doi.org/10.1016/J.JPHOTOCHEM.2016.09.031.

Kar, F., Hacıoğlu, C., Göncü, Y., Söğüt, İ., Şenturk, H., Burukoğlu Dönmez, D., Kanbak, G., Ay, N., 2021. In vivo assessment of the effect of hexagonal boron nitride nanoparticles on biochemical, histopathological, oxidant and antioxidant status. J. Clust. Sci. 32, 517–529. https://doi.org/10.1007/S10876-020-01811-W/METRICS.

Kay, A., Cesar, I., Grätzel, M., 2006. New benchmark for water photooxidation by nanostructured α-Fe 2O3 films. J. Am. Chem. Soc. 128, 15714–15721. https://doi.org/10.1021/JA064380L/ASSET/IMAGES/MEDIUM/JA064380LN00001.GIF.

Khan, S., Noor, T., Iqbal, N., Yaqoob, L., 2024. Photocatalytic dye degradation from textile wastewater: a review. ACS Omega 9, 21751–21767. https://doi.org/10.1021/ACSOMEGA.4C00887/ASSET/IMAGES/LARGE/AO4C00887_0007.JPEG.

Khurram, R., Nisa, Z.U., Javed, A., Wang, Z., Hussien, M.A., 2022. Synthesis and characterization of an α-Fe2O3-decorated g-C3N4 heterostructure for the photocatalytic removal of MO. Molecules 2022 27, 1442. https://doi.org/10.3390/MOLECULES27041442. Page 1442 27.

Kumar, Y., Kumar, R., Raizada, P., Khan, A.A.P., Singh, A., Van Le, Q., Nguyen, V.H., Selvasembian, R., Thakur, S., Singh, P., 2022. Current status of hematite (α-Fe2O3) based Z-scheme photocatalytic systems for environmental and energy applications. J. Environ. Chem. Eng. 10, 107427. https://doi.org/10.1016/J.JECE.2022.107427.

Liu, L., Fu, S., Lv, X., Yue, L., Fan, L., Yu, H., Gao, X., Zhu, W., Zhang, W., Li, X., Zhu, W., 2020. A gas sensor with Fe2O3 nanospheres based on trimethylamine detection for the rapid assessment of spoilage degree in fish. Front. Bioeng. Biotechnol. 8, 567584. https://doi.org/10.3389/FBIOE.2020.567584/BIBTEX.

Liu, J., Hui, D., Lau, D., 2022. Two-dimensional nanomaterial-based polymer composites: fundamentals and applications. Nanotechnol. Rev. 11, 770–792. https://doi.org/10.1515/NTREV-2022-0041/ASSET/GRAPHIC/J_NTREV-2022-0041_FIG_001.JPG.

Madi, K., Agueniou, F., Chebli, D., Tahraoui, H., Bouguettoucha, A., Zhang, J., Amrane, A., 2025. Polyaniline-modified iron and copper Co-doped cerium oxide nanocomposites for enhanced photocatalytic degradation of methylene blue: synthesis, and characterization. Colloids Surf. A Physicochem. Eng. Asp. 712, 136469. https://doi.org/10.1016/J.COLSURFA.2025.136469.

Mani, D., Mathivanan, D., Chang, H., Sakthivel, K., Elangovan, E., Sivakumar, T., Arivanandhan, M., Jayavel, R., 2020. A facile synthesis of novel ε-Fe2O3 grafted 2D h-BN nanostructures for enhanced visible active photocatalytic applications. N. J. Chem. 44, 12289–12298. https://doi.org/10.1039/D0NJ02321C.

Mohammed, W., Matalkeh, M., Al Soubaihi, R.M., Elzatahry, A., Saoud, K.M., 2023. Visible light photocatalytic degradation of methylene blue dye and pharmaceutical wastes over ternary NiO/Ag/TiO2 heterojunction. ACS Omega 8, 40063–40077. https://doi.org/10.1021/ACSOMEGA.3C01766/ASSET/IMAGES/LARGE/AO3C01766_0012.JPEG.

Nakamoto, K., 2008. Infrared and Raman spectra of inorganic and coordination compounds: part a: theory and applications in inorganic chemistry: sixth edition. Infrared Raman Spect. Inorg. Coord. Comp. Part A Theo. Appl. Inorg. Chem. Sixth Edn. 1–419. https://doi.org/10.1002/9780470405840.

A.H. Navidpour, M.B. Ahmed, J.L. Zhou, Photocatalytic degradation of pharmaceutical residues from water and sewage effluent using different TiO2 nanomaterials, Nanomaterials 2024, Vol. 14, Page 135 14 (2024) 135. https://doi.org/10.3390/NANO14020135.

Pakdel, A., Bando, Y., Golberg, D., 2014. Nano boron nitride flatland. Chem. Soc. Rev. 43, 934–959. https://doi.org/10.1039/C3CS60260E.

Ren, J., Innocenzi, P., 2021. 2D boron nitride heterostructures: recent advances and future challenges. Small Struct. 2, 2100068. https://doi.org/10.1002/SSTR.202100068;PAGE:STRING:ARTICLE/CHAPTER.

Sharma, P., Kumar, A., Dhiman, P., Sharma, G., Wang, T., García-Penas, A., Lai, C.W., 2025. Recent advances and perspective in Boron Carbon Nitride and Boron Nitride based materials for photocatalytic energy and environmental applications. J. Water. Process. Eng. 70, 106896. https://doi.org/10.1016/J.JWPE.2024.106896.

Sheng, W., Yu, X., Jia, X., Song, H., 2018. Sandwich-like porous α-Fe2O3 nanorod arrays/hexagonal boron nitride nanocomposites with improved high-temperature gas sensing. J. Mater. Sci. Mater. Electron. 29, 11236–11246. https://doi.org/10.1007/S10854-018-9210-1/METRICS.

Shenoy, M.R., Ayyasamy, S., Bhojan, V., Swaminathan, R., Raju, N., Senthil Kumar, P., Sasikumar, M., Kadarkarai, G., Tamilarasan, S., Thangavelu, S., Reddy, S.J.M.V., 2021. Visible light sensitive hexagonal boron nitride (hBN) decorated Fe2O3 photocatalyst for the degradation of methylene blue. J. Mater. Sci. Mater. Electron. 32, 4766–4783. https://doi.org/10.1007/S10854-020-05215-4/METRICS.

M. Shiraishi, M. Inagaki, X-ray diffraction methods to study crystallite size and lattice constants of carbon materials, carbon alloys: novel concepts to develop carbon science and technology (2003) 161–173. https://doi.org/10.1016/B978-008044163-4/50010-3.

Sivula, K., Le Formal, F., Grätzel, M., 2011. Solar water splitting: progress using hematite (α-Fe2O3) photoelectrodes. ChemSusChem 4, 432–449. https://doi.org/10.1002/CSSC.201000416.

Tarrio, C., Schnatterly, S.E., 1989. Interband transitions, plasmons, and dispersion in hexagonal boron nitride. Phys. Rev. B 40, 7852. https://doi.org/10.1103/PhysRevB.40.7852.

Tay, R.Y., Wang, X., Tsang, S.H., Loh, G.C., Singh, R.S., Li, H., Mallick, G., Tong Teo, E. H., 2014. A systematic study of the atmospheric pressure growth of large-area hexagonal crystalline boron nitride film. J. Mater. Chem. C. Mater. 2, 1650–1657. https://doi.org/10.1039/C3TC32011A.

Watanabe, K., Taniguchi, T., Kanda, H., 2004. Direct-bandgap properties and evidence for ultraviolet lasing of hexagonal boron nitride single crystal. Nat. Mater. 3, 404–409. https://doi.org/10.1038/NMAT1134;KWRD=MATERIALS+SCIENCE.

Yang, X., Sun, H., Zhang, L., Zhao, L., Lian, J., Jiang, Q., 2016. High efficient photo-fenton catalyst of α-Fe2O3/MoS2 hierarchical nanoheterostructures: reutilization for supercapacitors. Sci. Rep. 2016 6:1 6, 31591. https://doi.org/10.1038/srep31591. -.

Young, K.M.H., Klahr, B.M., Zandi, O., Hamann, T.W., 2013. Photocatalytic water oxidation with hematite electrodes. Catal. Sci. Technol. 3, 1660–1671. https://doi.org/10.1039/C3CY00310H.

Zhang, K., Feng, Y., Wang, F., Yang, Z., Wang, J., 2017. Two dimensional hexagonal boron nitride (2D-hBN): synthesis, properties and applications. J. Mater. Chem. C Mater. 5, 11992–12022. https://doi.org/10.1039/C7TC04300G.

Zhang, H.X., Shin, B.G., Lee, D.E., Yoon, K.B., 2020a. Preparation of PP/2D-nanosheet composites using MoS2/MgCl2- and BN/MgCl2-bisupported Ziegler-Natta catalysts. Catalysts 2020, Vol. 10, Page 596 10, 596. https://doi.org/10.3390/CATAL10060596.

Zhang, B.T., Wang, Q., Zhang, Y., Teng, Y., Fan, M., 2020b. Degradation of ibuprofen in the carbon dots/Fe3O4@carbon sphere pomegranate-like composites activated persulfate system. Sep. Purif. Technol. 242, 116820. https://doi.org/10.1016/J.SEPPUR.2020.116820.

J. Zhang, X. Jiang, M. Gong, Y. Zheng, Z-scheme Fe2O3/g-C3N4 heterojunction with excellent photocatalytic property, (2026) https://Doi.Org/10.1117/1.JPE.10.02350910(2020)023509.

Zhou, J., Duo, F., Wang, C., Chu, L., Zhang, M., Yan, D., 2022. Robust photocatalytic activity of two-dimensional h-BN/Bi 2 O 3 heterostructure quantum sheets. RSC Adv. 12, 13535–13547. https://doi.org/10.1039/D2RA02115C.